Enabling Fast and Accurate Neutral Atom Readout through Image Denoising

Chaithanya Naik Mude Department of Computer Sciences, University of Wisconsin–Madison Madison, WI, USA

Kunal Sinha Department of Physics, University of Wisconsin–Madison Madison, WI, USA Linipun Phuttitarn
Department of Physics, University of
Wisconsin–Madison
Madison, WI, USA

Mark Saffman
Department of Physics, University of
Wisconsin–Madison
Madison, WI, USA
Infleqtion, Inc.
Madison, WI, USA

Satvik Maurya
Department of Computer Sciences,
University of Wisconsin–Madison
Madison, WI, USA

Swamit Tannu Department of Computer Sciences, University of Wisconsin–Madison Madison, WI, USA

Abstract

Neutral atom quantum computers hold promise for scaling up to hundreds of thousands of qubits, but their progress is constrained by slow qubit readout. Measuring qubits currently takes milliseconds—much longer than the underlying quantum gate operations—making readout the primary bottleneck in deploying quantum error correction. Because each round of QEC depends on measurement, long readout times increase cycle duration and slow down program execution.

Reducing the readout duration speeds up cycles and reduces decoherence errors that accumulate while qubits idle, but it also lowers the number of collected photons, making measurements noisier and more error-prone. This tradeoff leaves neutral atom systems stuck between slow but accurate readout and fast but unreliable readout.

We show that image denoising can resolve this tension. Our framework, GANDALF, uses explicit denoising using image translation to reconstruct clear signals from short, low-photon measurements, enabling reliable classification at up to $1.6\times$ shorter readout times. Combined with lightweight classifiers and a pipelined readout design, our approach both reduces logical error rate by up to $35\times$ and overall QEC cycle time up to $1.77\times$ compared to state-of-the-art CNN-based readout for Cesium (Cs) Neutral Atom arrays.

1 Introduction

Neutral atom quantum computers have emerged as a promising platform for building scalable quantum systems. In recent years, they have demonstrated the ability to trap and control thousands of individual atoms—with systems reaching up to 3,000 qubits [5]. These systems are also making progress towards fault tolerance [28], with successful demonstrations of quantum error correction (QEC)[4], and are experimentally demonstrating applications in areas such as analog quantum simulation[3], and optimization [14].

Despite these advancements, a major challenge for neutral atom platforms is their relatively slow operation speeds.

Table 1 summarizes the typical durations of key operations—including two-qubit gates, single-qubit gates, readout, and full QEC cycles for leading quantum error correction codes—for systems from QuEra and various academic labs. For reference, we also show the operational latency for Google's superconducting hardware.

A large fraction of the total time during fault-tolerant quantum computing is spent on readout, as *qubit readout is the slowest and most error-prone step*, which not only limits the speed but also significantly impacts the error suppression capabilities of the quantum error correction code.

Why is readout slow in neutral atom architectures? In neutral atom systems, all atoms in the array are illuminated with a laser. If a qubit is in state $|1\rangle$, it will scatter photons; if it is in state $|0\rangle$, it will remain dark. These scattered photons are collected by a highly sensitive camera to determine each qubit's state. However, each atom emits only a small number of photons, and the optics can only collect a small fraction of them.

Table 1. Operational latencies for superconducting [1] versus neutral-atom quantum processors [33].

Hardware Platform	Two Qubit Latency	Readout Latency	Readout Fraction in QEC Cycle
Google	34 ns	500 ns	~0.5
QuEra	400 ns	10 ms	~0.75

To measure a qubit accurately, the system needs to collect more photons from the atom. It can do this by either increasing the laser power or extending the exposure time. Increasing the power risks overheating the atom, which can cause it to escape its trap, or jump to an unwanted energy level, or experience crosstalk. The other option is extending the exposure to collect more photons, but this slows down readout. As a result, the system faces a trade-off: faster measurements collect fewer photons and are less reliable, while slower measurements improve accuracy but take more time.

1

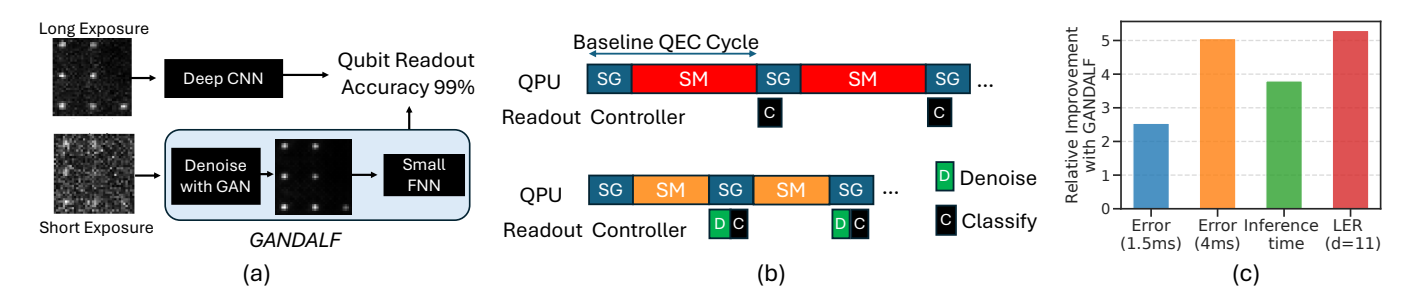


Figure 1. (a) GANDALF Design Overview. (b) Pipelining Readout Inference for baseline and GANDALF when running QEC cycle with Syndrome Generation (SG), Syndrome Measurement (SM), state Classification (C) and Denoising (D) stages. (c) Relative Improvement in Readout Fidelity, Inference Time, and Logical Error Rate (LER) for surface code patch, with code distance 11, compared to baseline design that uses deep CNN [25].

Ideally, we want fast readout without using high laser power, which translates to doing classification at significantly low photon counts. Most existing readout classifiers [25] rely on high photon counts to distinguish between qubit states. Higher photon counts create a clear separation between $|0\rangle$ and $|1\rangle$ states. But this assumption breaks down for fast, low photon count measurements, where classical classifiers struggle to maintain the same level of accuracy. This limitation presents a significant bottleneck for enhancing QEC, calibration, and application-level performance.

In this work, we demonstrate that denoising can enable high-fidelity readout even at low photon counts and can be effectively used for accelerating the readout for neutral atom quantum computers. We utilize a dataset of paired fluorescence images from a 3 × 3 Cesium (Cs) atom array, where a high Signal to Noise Ratio (SNR) path provides long-exposure ground truth labels and an attenuated path produces noisy, short-exposure measurements [25]. We observe that conventional CNN classifiers, effective in natural-image domains experience degraded performance because bright and dark histograms overlap and neutral atom images lack semantic richness. This motivates a different approach of processing the noisy images prior to classification to improve the SNR by filtering the noise, instead of classifying them directly.

Our central design insight is to decouple signal recovery from classification. We introduce GANDALF, a generative adversarial framework that denoises low-photon images, restoring per-site fidelity and suppressing photon noise and crosstalk. By training on paired datasets of low-and high-photon fluorescence frames from cesium atom arrays [25], our approach reconstructs high-fidelity images from fast, low-photon measurements—enabling rapid and accurate qubit state classification. Figure 1 shows that GAN can significantly improve the signal-to-noise ratio for a short-exposure atom array image, enabling high-fidelity readout even at low photon counts.

Moreover, with denoising, the classification task becomes far easier, enabling the use of lightweight site-specific models such as feedforward networks or matched filter hybrids. These compact classifiers match the accuracy of larger CNNs while cutting latency by up to five times and parameter count by more than an order of magnitude, making them practical for arrays with thousands of qubits. Equally important, we propose the readout pipeline to overlap classification with image acquisition. By pipelining these stages, classification adds only once to total latency rather than every cycle, eliminating it as a recurring bottleneck as shown in Figure 1(b). Pipelining of readout denoising and classification enables room for using sophisticated ML models that can maintain high accuracy with low SNR to reduce readout time.

Finally, by making the denoising model fully convolutional, the same network trained on small calibration arrays seamlessly generalizes to larger lattices, maintaining per-site inference cost nearly constant as system size grows. This is crucial as generating fully occupied qubit lattices can be slow experimentally due to slow loading.

Our evaluations show that this combination of denoising GAN and a lightweight classifier, such as a shallow Feed Forward Neural Network (FNN), delivers significant gains. At 1.5ms exposures, GANDALF reduces readout error by 2.8× compared to CNN baselines. The dataset we use is imperfect, and we expect higher-quality data to be available in the near future. Therefore, to understand the best-case improvements with denoising, we create a dataset generated via confidencebased filtering, and on this smaller post-selected dataset, we observe sub-1% inaccuracy even at the shortest duration of 1.5ms. This highlights the effectiveness of our approach in reducing readout duration to the sub-millisecond region for Cs atom arrays. At the system level, logical error rates improve dramatically—up to 35× reduction for bivariate bicycle codes and 5× for surface codes—demonstrating that faster, denoised readout directly strengthens fault tolerance. Lightweight classifiers achieve inference in the 100 µs range, and pipelining shortens overall QEC cycle time by 1.77×, reducing idling-induced decoherence. Even with commodity GPUs with 4K CUDA cores, the denoiser scales from 3×3 to 64×64 and even larger arrays with sublinear growth in latency, ensuring feasibility for next-generation processors. This paper makes the following contributions:

- We demonstrate denoising enables reliable state discrimination at much shorter exposure times, making low-photon and pipelined readouts viable for fault-tolerant execution.
- By adapting generative networks to the unique structure of fluorescence snapshots, we show GAN-based denoising outperforms conventional CNNs in the low-SNR regime.
- Our fully convolutional framework maintains per-site fidelity while effectively suppressing noise and crosstalk, and it generalizes robustly from small calibration arrays to large-scale atom lattices.
- GANDALF reduces readout error by up to 2.5×, lowers logical error rates up to 5× for surface code and up to 35× for BB code, and shortens QEC cycle time by 1.77×, directly addressing readout bottleneck in neutral atom quantum computers.

2 Background

2.1 Neutral atom quantum computing

Neutral atom platforms have emerged as a promising architecture for scalable quantum computing, offering flexible qubit layouts, long coherence times, and high connectivity, [26, 34]. In these systems, individual atoms—typically species such as Rubidium (Rb), Cesium (Cs), Strontium (Sr), or Ytterbium (Yb)—serve as qubits, with internal electronic or hyperfine states encoding the logical $|0\rangle$ and $|1\rangle$ states.

Qubits are held in space using optical tweezers: tightly focused laser beams that create potential wells to trap single atoms. Arrays of tweezers are generated using acousto-optic deflectors or spatial light modulators, allowing dynamic reconfiguration and parallel operation. The vacuum environment and tight localization of atoms enable long coherence times, while high-numerical-aperture lenses allow for high-fidelity optical control and measurement.

Single-qubit gates are implemented using resonant laser or microwave pulses that drive coherent rotations between the two qubit states. Recent experiments [22, 34] performed these operations in parallel across the array, with gate fidelities exceeding 99.5%. Two-qubit entangling gates are typically realized via the Rydberg blockade mechanism: atoms are excited to high-energy Rydberg states where strong dipole-dipole interactions prevent simultaneous excitation of nearby qubits [16, 19]. This interaction enables fast, high-fidelity two-qubit gates with interaction ranges spanning several micrometers, making neutral atom systems especially well-suited for two-dimensional lattice-based quantum error correction codes and programmable quantum simulations.

2.2 Readout in neutral atom architecture

In neutral atom quantum computers, readout relies on detecting whether an atom is in a particular internal state. These qubit states are typically encoded in long-lived hyperfine

or electronic levels, and readout works by shining a laser tuned to excite only one of the qubit states. If the atom is in the excited state (e.g., $|1\rangle$), it will scatter photons and appear bright under a camera. If it is in the other state (e.g., $|0\rangle$), it remains dark. By capturing this fluorescence with a sensitive camera, the system determines the atom's state.

Although conceptually simple, this readout process is slow compared to the speed of quantum gates. To confidently distinguish between bright and dark states, the system must collect enough photons to overcome background noise and random fluctuations. This requires either using a stronger laser or increasing the exposure time. A stronger laser can cause heating, which may knock the atom out of its trap or excite it to unwanted energy levels. On the other hand, a longer exposure slows down the readout and limits how quickly quantum circuits can be executed.

Additionally, the fidelity of readout depends on many experimental parameters, including the numerical aperture of the imaging system, the qubit species, and spacing between atoms. For example, atoms placed closely together can interfere with each other, a problem known as crosstalk. To mitigate these issues, researchers are exploring advanced methods such as machine learning and denoising techniques to improve readout fidelity at shorter measurement times.

Overall, while readout is essential for extracting useful information from a quantum computer, its speed and reliability pose a major challenge for scaling up neutral atom systems and supporting fast feedback in quantum error correction.

2.3 Why does fast readout matter?

The execution time of a fault-tolerant quantum program can be coarsely approximated as:

ExecTime
$$\approx$$
 (#T-Gate) \times (*d*-rounds) \times (QEC Cycle Time) (1)

Each component in this model encapsulates a key bottleneck to scalable, fault-tolerant quantum computation:

- Non-Clifford Gates (e.g., *T* gates) are necessary for universal quantum computation. They are the slowest operations due to magic state distillation [13].
- *d*-Rounds represent the number of QEC iterations needed to suppress logical errors for a code of distance *d*. As expected, larger *d* values are required for lower physical error rates, increasing overall runtime.
- QEC cycle time is the duration of one round of quantum error correction, where errors are detected and corrected to keep logical qubits free of errors.

We observe, for most qubit technologies the duration of each QEC cycle is fundamentally bounded by the time it takes to measure qubits and reinitialize them—two steps that are dominated by readout latency in neutral atom systems:

While this model emphasizes the linear relationship between readout latency and QEC cycle duration, it omits other crucial—but often overlooked—roles that fast readout plays in the performance of neutral atom quantum computers:

Atom loading and rearrangement overhead. In neutral atom platforms, building a defect-free 2D qubit lattice requires stochastic loading followed by iterative rearrangement. This initialization process is slow, imaging intensive, and requiring repeated fluorescence-based measurements to identify occupied sites and reposition atoms using optical tweezers. Fast, high-fidelity readout accelerates each stage of this pipeline—enabling denser lattices, reducing the probability of atom loss during relocation, and improving experiment yield. Though often hidden behind "setup time," inefficiencies here can dominate runtime in large-scale systems or in hybrid pipelines where reloading is triggered adaptively.

QEC bootstrapping and syndrome verification. Initialization is not limited to loading alone. For QEC codes to start correctly, ancilla qubits must be verified through measurement. Faster readout enables quicker feedback, reducing dead time and improving the throughput of syndrome generation across the code lattice.

Pipelining and reuse of physical infrastructure. In principle, multiple Magneto-Optical Traps (MOTs) can be deployed in parallel to mask atom loading time, but doing so increases system complexity, cost, and physical footprint. Faster readout alleviates the need for deep pipelining by making each MOT pass more productive, reducing the amortized cost per qubit and easing scalability constraints.

While readout speed directly governs QEC cycle time, its influence is far broader—impacting lattice preparation, code startup, and system utilization efficiency. Fast readout is not just a lever for shorter execution times; it is a key enabler for practical, reliable, and reconfigurable fault-tolerant quantum computing on neutral atom platforms.

3 Challenges in Neutral Atom Readout

3.1 State of the art

Oubit readout remains a key bottleneck in neutral atom quantum computing, with significant variations in fidelity and speed across available atomic species, including Cesium (Cs), Rubidium (Rb), Ytterbium (Yb), and Strontium (Sr) illustrated in Figure 2. The performance of fluorescence-based state detection depends strongly on species-specific properties such as cycling transition strength, background scattering, and susceptibility to state leakage. For instance, alkalineearth(-like) atoms such as Yb and Sr offer narrow-line transitions that support high-fidelity imaging with minimal atom loss [22, 29], but they often require cryogenic cooling and complex laser systems. In contrast, alkali atoms like Cs and Rb are experimentally simpler to trap and manipulate, but their readout typically involves trade-offs between speed, fidelity, and trap loss due to heating and off-resonant scattering [8, 25]. Improving readout performance across all

species is crucial for supporting quantum error correction, which relies on fast and repeated measurements of ancilla qubits. Each atomic species imposes distinct system-level constraints such as photon budget, trap spacing, and detection optics necessitating a careful balance between fidelity, speed, hardware complexity, and scalability.

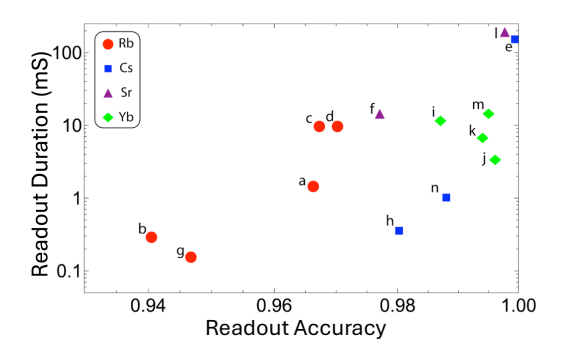


Figure 2. State of the art in neutral atom readout latency vs readout fidelity for Cesium(Cs) [6, 25, 35], Rubidium(Rb) [9, 11, 18, 23, 30], Strontium (Sr) [7, 31], and Ytterbium (Yb) [15, 20, 21, 24] qubits. Data originally collected by [27].

3.2 Experimental setup and dataset

In this work, we explore the advantages of employing machine learning to improve the accuracy and speed of measuring qubits in a neutral atom quantum computer. The researchers use a 3×3 grid of cesium atoms, each held in place by optical tweezers. To read out the state of each atom, they shine laser light that causes atoms in the "bright" state to fluorescence, while "dark" state atoms emit little to no light. The emitted light is captured by a sensitive camera through two optical paths: a bright, high-quality path used for generating accurate labels, and a dimmer, noisier path used for testing machine learning models.

The experimental setup is shown in Figure 3, uses an EMCCD camera to capture the photons emitted by the atom due to fluorescence. The primary path captures entire signal, i.e, photons emitted by the atom during the fluorescence, while the secondary path attenuates this signal by $10\times$ resulting in equivalent shorter exposure setting, leading to $10\times$ reduction in readout time. The difference is evident from the histograms shown in the Figure 3, where the long exposure images shows the histograms with better separation relative to short exposure images.

The authors developed two convolutional neural networks (CNNs) to classify the atom states from images. The first, CNN-site, looks at one atom at a time. The second, CNN-array, processes the full 3×3 image and can account for light spillover (crosstalk) between neighboring atoms—an issue that worsens when atoms are spaced closely together.

They trained the CNNs on labeled data from the highquality path and tested them on the noisy images. Compared to standard threshold-based methods, both CNNs achieved significantly lower error rates. CNN-site reduced errors by up to 56% in low-crosstalk settings, while CNN-array cut errors by up to 43% and crosstalk by 78% in tightly packed arrays relative to Gaussian thresholding.

Overall, the machine learning models allows faster readout while maintaining high accuracy—an important step toward real-time qubit measurement in scalable quantum systems.

3.3 Why are standard CNN models not enough?

CNNs are the de-facto models for image classification. In natural-image domains with rich semantic content and large training datasets, they perform remarkably well, even in the presence of moderate image noise, label noise, and variations in scale or rotation, as they learn robust, hierarchical representations of visual features.

CNNs operate by first detecting local, low-level features such as edges, corners, and textures in early convolutional layers. Deeper layers combine these primitives into higher-level features that capture complex shapes and semantic structure. This feature hierarchy allows CNNs to distinguish objects even under degraded imaging conditions, provided there is enough semantic variation in the data.

Neutral atom qubit readout images differ fundamentally from natural-image datasets. Each image consists of fluorescence from atoms arranged on a fixed lattice, where each site is either bright ($|1\rangle$) or dark ($|0\rangle$). Short exposure measurements capture roughly ten times fewer photons than long-exposure images, resulting in significantly lower SNR, as shown in Figure 4(a)–(b). The corresponding pixel-intensity histograms in Figure 4(c)–(d) illustrates this effect of bright and dark sites overlapping heavily at short exposures, while long exposures yield well-separated distributions, making accurate state discrimination difficult for low-SNR images.

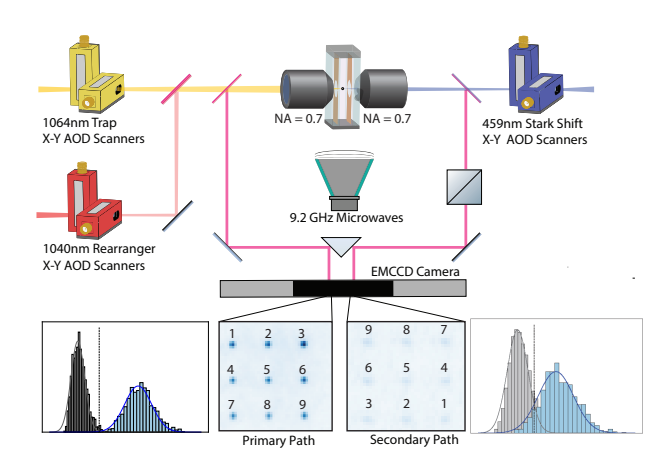


Figure 3. Experimental setup[25] for obtaining long (primary) and short (secondary) exposure readout images.

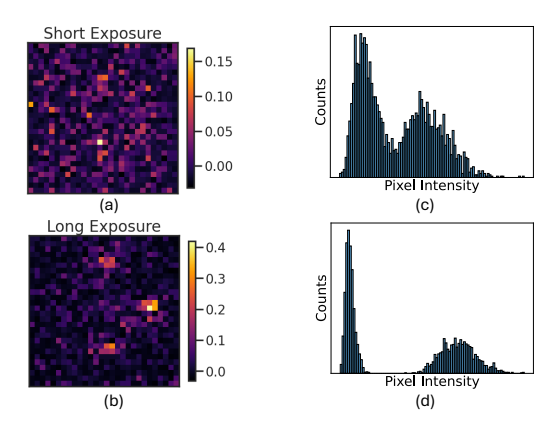


Figure 4. (a)-(b) Visualization and (c)-(d) histogram of pixel intensity of a site of short exposure (attenuated secondary path) and long exposure images respectively.

Unlike natural images, neutral atom readouts lack semantic structure and variability. The information needed for classification is localized to fixed, small patches around lattice sites, meaning that one of CNNs' primary advantages—spatial invariance—offers little benefit. In fact, enforcing invariance can hinder performance by encouraging the model to search for features that are not physically meaningful in this highly constrained setting.

The challenge is amplified by the difficulty of collecting large, clean training datasets. Neutral atom readout is inherently slow, and acquiring images at scale is time-consuming. The process can also introduce label noise due to state preparation or measurement errors, further reducing the effectiveness of supervised training. As a result, models must learn from limited and imperfect data, unlike in typical vision benchmarks with millions of labeled examples are available.

These limitations become critical at low signal-to-noise ratio (SNR), where the photon count distributions for bright ($|1\rangle$) and dark ($|0\rangle$) states overlap due to noise sources such as photon shot noise and camera readout noise. In this regime, the local intensity patterns that CNNs learn to detect the signal become statistically indistinguishable from random noise fluctuations. Consequently, the network struggles to maintain discriminability between qubit states.

4 Enabling Readout for Low Photon Counts

In neutral atom systems, qubit readout uses site-resolved fluorescence imaging, where each atom site's pixel intensity reflects the number of scattered photons collected during a finite illumination period. The detected signal scales linearly with integration time, while dominant noise sources, such as shot noise and camera sensor noise, grow proportionally to the square root of integration time. Therefore, shorter exposures incur a steep drop in SNR, degrading readout fidelity. Longer exposures improve the SNR but risk heating

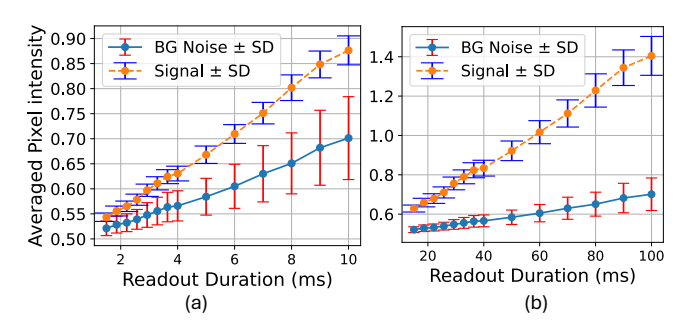


Figure 5. Comparing background noise and signal strength across readout durations for (a) Short exposure images from 1.5ms to 10ms, (b) Long exposure images from 15ms to 100ms.

atoms, increasing loss rates and adding latency, thus creating a fundamental trade-off between speed and accuracy.

Figure 5 shows the scaling mismatch enhances the signal relative to background noise more rapidly with increase in readout duration. Long exposures push occupied-site intensities well above the background noise, enabling even simple thresholding to achieve high accuracy. In short exposures, intensities approach the noise floor, causing bright and dark site distributions to overlap and masking spatial features critical for downstream classification tasks.

4.1 Improving signal-to-noise ratio

In the low-photon regime, effective denoising is essential for recovering and preserving the discriminative features needed to achieve high accuracy in downstream classification. Conventional techniques such as Gaussian smoothing, median filtering, or Wiener filtering can be effective under moderate noise conditions, where they reduce noise by averaging or selectively filtering image components. However, when noise levels approach the signal amplitude these methods often fail. They tend to blur fine spatial details and distort the point-spread patterns that characterize each site's intensity, thereby removing the critical features required for reliable classification. In such cases, traditional filtering leaves downstream classifiers with insufficient information to accurately distinguish between occupied and unoccupied sites.

Generative approaches offer a more powerful alternative by learning a direct mapping from low-SNR (short exposure) to high-SNR (long exposure) images. Using paired experimental datasets, these models can exploit the repetitive lattice structure of neutral atom arrays, preserve per-site correlations, and selectively enhance meaningful features while suppressing noise, thereby framing the task as an image-to-image translation problem.

Conditional generative adversarial networks (cGANs), such as Pix2Pix, are well-suited for the image-to-image translation problems [17]. The generator restores missing spatial details, recovers contrast between bright (occupied) and dark (unoccupied) sites, and enhances fine-scale structure, while

the discriminator acts as a critic to ensure that the generated outputs are consistently close to the true high-photon-count counterparts as shown in Figure 6(a). These models produce denoised images with the resolution and contrast required for accurate downstream classification in the low-photon regime as shown in Figure 6(b).

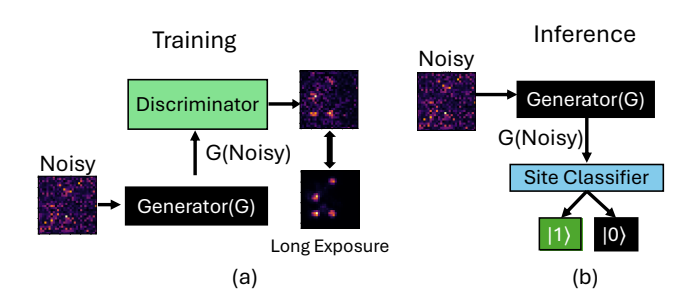


Figure 6. (a) GAN Training; (b) Inference with learned generator and downstream readout classification.

Figure 7 shows generative denoising improving low-SNR short-readout images (a) toward the clear site separation of long-exposure images (b), with (c) recovering much of the lost contrast. Figure 7(d) and (e) compare site-averaged intensities with the long-exposure reference. Correctly denoised sites fall in Q1 (bright-bright) and Q3 (dark-dark), whereas Q2 (bright-dark) and Q4 (dark-bright) indicate mismatches. In Figure 7(d), noise scatters many points into Q2 and Q4, but in Figure 7(e) denoising pulls them back into Q1 and Q3, showing closer agreement with ground truth and fewer mismatches. By improving effective SNR without altering the physical readout process, generative denoising directly enhances classification accuracy in low-photon regime, lowering logical error rates and reducing the error-correction overhead in large-scale quantum processors.

4.2 Deep-dive into generative models for denoising

While state-of-the-art generative models for image-to-image translation, such as Pix2Pix, have demonstrated impressive results in the natural-image domain, directly applying them to neutral atom readout is non-trivial. Natural-image datasets contain rich semantic diversity, i.e, edges, textures, and object boundaries, that models can exploit to learn generalizable mappings. In contrast, neutral atom images consist of highly repetitive, lattice-aligned point-spread patterns with relatively few distinguishing features beyond site intensity. This lack of semantic richness means that large, general-purpose models often allocate capacity to irrelevant structures, learn spurious correlations, or overfit to limited noise patterns. The challenge is compounded by the fact that dataset sizes in neutral atom experiments are orders of magnitude smaller than typical computer vision benchmarks, limiting the effectiveness of data-intensive GAN based denoising architectures.

In this setting, the goal of denoising is not to produce visually pleasing images in a perceptual sense but to maximize per-site classification fidelity. Each lattice site must be reconstructed as close as possible to its high-SNR counterpart, and spatial separation between neighboring sites must be preserved to avoid "blob merging" that can distort site-to-site correlation. Achieving this requires a model that emphasizes local structural accuracy and preserves the repetitive lattice geometry, rather than one optimized for global realism.

To meet these requirements, we developed a custom conditional GAN framework, GANDALF (Generative Adversarial Network for Denoising At Low Fluorescence) as shown in Table 2. We employ similar structure as Pix2Pix architecture, but tailor it to learn the mapping from low-SNR to high-SNR images of neutral atom readout. The generator follows an encoder-bottleneck-decoder design with skip connections and residual blocks, combining stability in training with strong feature preservation. Skip connections help mitigate vanishing gradients in deeper networks, allowing early-layer features to directly influence the final reconstruction, which is important for retaining high-frequency spatial detail that might otherwise be lost during downsampling. Residual blocks in the bottleneck further improve feature retention and stability by refining representations without disrupting the preserved information.

Training optimizes a combination of adversarial loss, which encourages realism, and a heavily weighted pixel-wise L1 loss, which enforces fidelity to the high-SNR target at each pixel. Training is performed using the Adam optimizer with

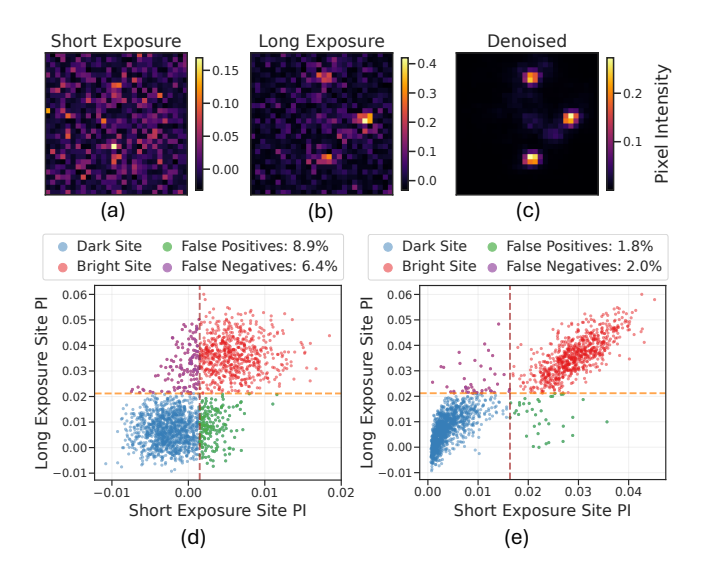


Figure 7. Normalized average pixel intensity for the same experiment corresponding to (a) Signal attenuated path (short exposure) (b) Primary path (long exposure) (c) Denoised image from short exposure image. Misclassifications for: (d) Short exposure, (e) Denoised.

Table 2. Generator and discriminator architectures

Layer	Filter shape	Output shape		
Generator				
Input	N/A	$H \times W \times 1$		
Enc1	$3 \times 3 \times 1 \times 64$	$H \times W \times 64$		
Enc2	$3 \times 3 \times 64 \times 128$	$H/2 \times W/2 \times 128$		
Enc3	$3 \times 3 \times 128 \times 256$	$H/4 \times W/4 \times 256$		
Res Block 1	$3 \times 3 \times 256 \times 256$	$H/4 \times W/4 \times 256$		
Res Block 2	$3 \times 3 \times 256 \times 256$	$H/4 \times W/4 \times 256$		
Res Block 3	$3 \times 3 \times 256 \times 256$	$H/4 \times W/4 \times 256$		
Dec3	$4 \times 4 \times 256 \times 128$	$H/2 \times W/2 \times 128$		
Dec2	$4\times4\times256\times64$	$H \times W \times 64$		
Dec1	$3 \times 3 \times 128 \times 1$	$H \times W \times 1$		
Discriminator				
Input	N/A	$H \times W \times 1$		
Conv1	$3 \times 3 \times 1 \times 64$	$H/2 \times W/2 \times 64$		
Conv2	$3 \times 3 \times 64 \times 128$	$H/4 \times W/4 \times 128$		
Conv3	$3 \times 3 \times 128 \times 256$	$H/8 \times W/8 \times 256$		
Conv4	$3 \times 3 \times 256 \times 512$	$H/16 \times W/16 \times 512$		
Output	$1\times1\times512\times1$	$1 \times 1 \times 1$		

parameters $\beta_1 = 0.5$ and $\beta_2 = 0.999$, a learning rate of 0.0002, batch size 16, and 30 training epochs.

The total generator loss is given by:

$$\mathcal{L}_{G} = \mathcal{L}_{GAN}(G, D) + \lambda_{L1} \mathbb{E}_{x, y} [\|G(x) - y\|_{1}]$$
 (3)

where x is the low-SNR input, y is the high-SNR target, \mathcal{L}_{GAN} measures how well the generator fools the discriminator, and λ_{L1} controls the trade-off between perceptual realism and pixel-level accuracy. In our experiments, $\lambda_{L1}=200$ provided a good balance between structural preservation and noise suppression. To further improve structural preservation, the objective can be augmented with SSIM (Structural Similarity Index) and PSNR (Peak Signal-to-Noise Ratio) terms, which reward reconstructions that maintain perceptual structure and maximize signal strength relative to noise.

4.3 Denoising limitations for neutral atom readout

In the low-SNR and low structural variability in readout images, GAN-based denoising can introduce systematic errors despite producing visually cleaner images. Overfitting to recurring noise patterns may distort true signal distributions, and in borderline cases where occupancy depends on subtle intensity differences, the generator may hallucinate sites or suppress faint signals, reducing reconstruction fidelity.

4.3.1 Mode collapse and data limitations. A common failure mode for generative models is mode collapse, where the generator outputs uniformly "bright" or "dark" patterns that satisfy the discriminator but fail to preserve true site occupancy. The repetitive lattice geometry and limited calibration datasets in atom readout increases chances, leading to memorization of noise or spurious correlations that introduce artificial features or suppress real signals. These errors directly degrade downstream classification, especially under unseen noise conditions.

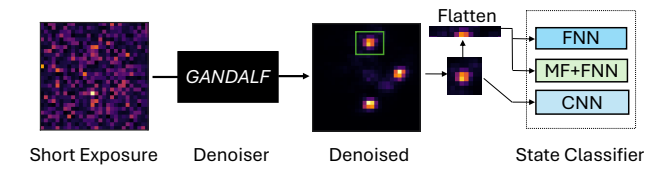


Figure 8. Overview of Readout Classification Methods.

4.4 Training strategies to mitigate failure modes

Mode collapse can be reduced by preventing the discriminator from becoming overconfident through label smoothing, i.e, assigning real samples a label of 0.9 instead of 1.0 and fake samples 0.1 instead of 0.0. We further reduce collapse and hallucination risk by updating the discriminator less frequently than the generator, giving generator more opportunity to refine outputs without being prematurely constrained.

Dropout in the discriminator encourages focus on robust, generalizable features rather than memorizing noise patterns. To promote smooth convergence and reduce oscillatory dynamics, cosine annealing learning rate schedules are employed. Finally, early stopping based on validation L1 loss captures the best model before it begins overfitting to training-set noise characteristics. Together, these measures allow the model to reliably reconstruct from low-SNR to high-SNR readouts without introducing artificial features, improving classification accuracy in the low-photon regime.

4.5 Downstream Readout Classification Task

Accurate readout classification is critical for high-fidelity state detection. Traditional thresholding approaches are lightweight but fragile in low-photon regimes. Matched filtering offers interpretability but similarly degrades at low SNR. CNN-based classifiers achieve higher accuracy at the cost of excessive complexity with $\sim 74M$ for 3×3 atom array [25], making impractical to scale them for larger atom arrays.

GANDALF mitigates this challenge by denoising short-exposure measurements, reducing classification hardness and enabling the use of lightweight models without sacrificing fidelity. The task of neutral atom readout is formulated as binary classification, i.e, given a fixed-size site-centered patch, determine whether the atom is bright-occupied ($|1\rangle$) or dark-unoccupied ($|0\rangle$). Each of the site-specific models are trained per lattice location to account for spatial variation in fluorescence and noise.

We design and evaluate matched filter with neural network (MF+NN), feedforward neural network (FNN), and 2D-CNN classifiers, to compare their strengths and limitations. Figure 8 illustrates the classification pipeline. The process begins with denoises the readout image with GANDALF, followed by extraction of fixed-size patches centered on each lattice site. CNNs operate directly on these patches, whereas

FNN and MF+NN use flattened patches. In case of MF+NN, matched-filter features are additionally incorporated.

Classifier improvement is measured using relative infidelity reduction $\eta=1-\delta_{\rm method}/\delta_{\rm CNN(Site)}$, where δ is classification inaccuracy, and higher η implies better inaccuracy reduction. As shown in Fig. 9, all classifiers benefit substantially from GANDALF, achieving over 60% reduction in inaccuracy relative to the baseline. At the shortest readout durations, error is reduced by 2.5×, while model size and inference latency decrease by up to 16.5× and 5× respectively, compared to the baseline. Similarly, end-to-end latency including GANDALF is 4× faster than the CNN(Array) baseline.

Among site-specific classifiers, FNN yields the highest accuracy gains, while MF+NN matches this performance with fewer parameters by exploiting matched-filter features, both surpassing baseline CNNs. Together with GANDALF, they deliver scalable, low-latency readout well-suited for fault-tolerant neutral atom architectures.

5 Scalable and Fast Readout for QEC

Supporting QEC at scale requires high-fidelity in-circuit measurements across hundreds or thousands of qubits. At such scales, readout speed is a primary bottleneck. While two-qubit gates finish in less than a microsecond, the current readout can take tens of milliseconds. To overcome this gap, two factors are critical: (1) Image acquisition — the duration needed to collect scattered photons. (2) Classification latency — the time required to process the signal and infer qubit states for thousands of qubits. Shorter image acquisition times reduce delay but make classification harder, and often demand more sophisticated models with higher inference costs. In this section, we analyze the speed–accuracy tradeoff and the scalability of GANDALF.

5.1 Scaling to larger atom arrays

As neutral atom systems scale to thousands of qubits, readout fidelity must remain robust across increasingly large arrays. A major challenge is that many denoising and classification approaches are tailored to fixed input dimensions, making them impractical for scaling without retraining or

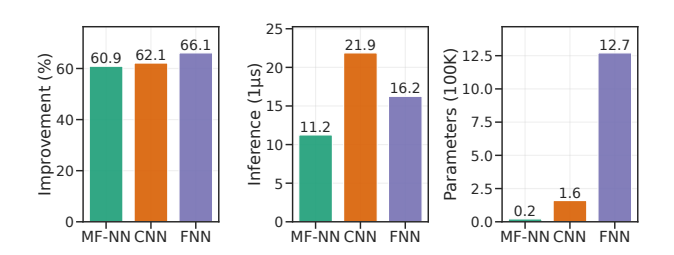


Figure 9. Comparison of readout classification methods. Metrics reported: relative infidelity reduction (η) compared to CNN(Site), inference time and total model parameters.

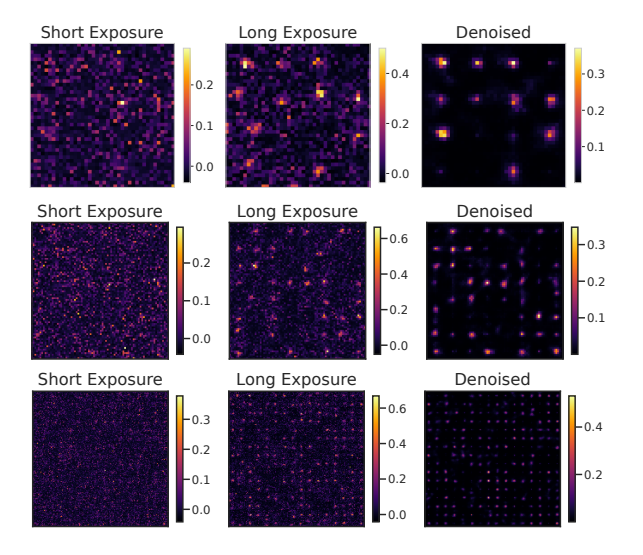


Figure 10. Scalability of GANDALF with consistent recovery of site contrast for atom arrays of $n \times n$ atoms for n = 4,8,16.

re-engineering. This creates concerns about computational load and consistency of performance at scale.

Our approach overcomes this by employing a fully convolutional denoising network, which naturally accepts images of arbitrary size. Convolutional filters operate locally and reuse the same learned kernels across space, allowing the model to generalize seamlessly from small calibration arrays to much larger lattices without modifying architecture or parameters. To evaluate scalability, we test GANDALF on synthetically generated large atom array images. We generate these by stitching single-atom images.

Table 3 reports PSNR, SSIM, and mean L1 loss for denoising as atom arrays scale from 4×4 to 64×64. The results show only slight degradation with increasing grid size, i.e, PSNR drops by less than 0.5dB, SSIM decreases by 0.02, and mean L1 loss remains nearly unchanged. With fixed Model complexity, the computational cost of GANDALF grows marginally with image size, keeping per-site inference time nearly constant.

Figure 10 shows the denoiser trained on 3×3 arrays generalizes to larger arrays upto 16×16 , while preserving bright–dark separation and site contrast. This demonstrates GANDALF trained on small arrays can transfer directly to large-scale neutral atom processors with thousands of atoms.

Table 3. Scalability of denoising across atom array sizes.

Metric	Grid Size $(n \times n)$			
Metric	4×4	8 × 8	32×32	64 × 64
PSNR (dB)	25.17	25.06	24.79	24.86
SSIM	0.3337	0.3368	0.3134	0.3187
Mean L1 loss	0.0362	0.0365	0.03701	0.0367
Latency(ms)	0.201	0.514	9.091	33.490

5.2 Denoising Latency and Practical Scalability

We evaluate the GANDALF generator (4.7M parameters) across grid sizes, batch sizes, and parallel executions to assess its suitability for real-time QEC pipelines. Although input size affects inference time, the fully convolutional design ensures sublinear growth on a single GPU, with latency remaining within tens of ms even for 32×32 arrays as shown in Table 3. These trends indicate that denoising is practical at scale, with GPUs or other accelerators.

Table 4. Denoising throughput (TP) with the batch sizes.

Metric	Batch Size				
Wietric	1	8	32	64	128
TP (img/s)	460.0	3330.3	9225.0	11721.4	12711.4
Latency (ms)	2.174	0.300	0.108	0.085	0.079

Table 5. Denoising throughput (TP) with the parallel models.

Metric	Parallel Models			
Wittit	4	8	16	32
TP/model (img/s)	10615.5	11204.0	11786.8	12083.5
Latency (ms)	0.094	0.089	0.085	0.083

Throughput can be further improved using batching and parallelism. With batching, the GPU processes multiple images simultaneously, reducing per-image latency from 2.174 ms to 0.079 ms at a batch size of 128 (Table 4). Parallel execution provides another dimension of scaling: as shown in Table 5, throughput per model remains nearly constant with latencies of 80– $90~\mu s$, while memory usage increases roughly linearly with the number of models. In practice, moderate batching combined with 8–32 concurrent models keeps denoising well within QEC timing budgets while sustaining high throughput. Because throughput aggregates and scales nearly linearly with the number of models, practical large-scale readout is achievable even on commodity GPU.

5.3 Pipelining classification across cycles

Readout, from image acquisition to state classification, must operate within the strict timing budget of QEC cycles. State preparation and rearrangement is performed to assemble defect-free atom arrays, before the start of error correction. Later, QEC proceeds through repeated cycles of gate execution, and measurement. As summarized in Table 6, gate operations are fast, but readout remains the dominant percycle bottleneck due to millisecond-scale image acquisition and the additional classification step.

In current approaches, classification is performed immediately after image acquisition, with inference latency accumulating at every QEC cycle as in Figure.10(a). While negligible for small systems, this overhead becomes significant as arrays scale to hundreds of qubits. Baseline methods typically

employ both single-site and multi-site CNN classifiers with classification taking upto $\sim 50\mu s$ per site, and 500 μs for a 3×3 array, respectively, almost an order of magnitude slower for multi-site. Similar scaling to larger arrays quickly drives classification into the multi-millisecond regime, creating a major throughput bottleneck.

Our approach mitigates this by relying on lightweight single-site classifiers such as FNNs and MF+NNs runs parallel across sites and achieve up to 5× faster inference than CNN(Array). Multi-site correlations are instead captured in the denoising stage, allowing classification to remain compact and scalable. Moreover, we propose pipelining classification with image acquisition to effectively hide its latency, eliminating it as a limiting factor for large-scale QEC.

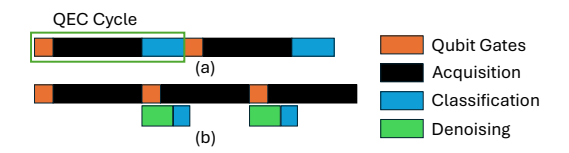


Figure 11. (a) Unpipelined, (b) Pipelined qubit readout.

In existing small-scale NA readout systems, classification is performed immediately after image acquisition to trigger reset and atom reloading, making it a per-cycle bottleneck. Recent works suggest the reset[10] and atom loss[2] can be tolerated. As chances of atom loss is rare and does not introduce spurious correlations, reloading can instead be deferred by one round, allowing classification to overlap with the next measurement as shown in Fig. 11(b). This reduces idle time and mitigates idling-induced errors.

With unpipelined design, time to execute *d* QEC rounds:

$$T_{\text{OEC}}^{\text{unpipelined}} = d \times (t_{\text{gate}} + t_{\text{readout}} + t_{\text{classification}}),$$
 (4)

In our scheme, the effective latency becomes

$$T_{\text{QEC}}^{\text{pipelined}} = d \times (t_{\text{readout}} + t_{\text{gate}}) + (t_{\text{denoise}} + t_{\text{classification}}), (5)$$

With pipelining, classification cost is incurred only after the final round, with most of its cost hidden behind acquisition. Gains are largest at short readout times (1.5 ms). Crucially, classification never becomes the limiting factor, ensuring OEC is constrained mainly by acquisition time.

Table 6. Typical QEC cycle latency for neutral-atom systems.

Process	Typical Duration	
State preparation (one-time)	~ 100 ms	
Two-qubit gate operation	few μ s	
Image acquisition	few ms	
Classification	few 100 μ s	

6 Methodology

Quantum hardware and dataset. We obtained datasets with the readout images from the 9-qubit neutral atom system mentioned in [25] with two different atom spacings as $5\mu m$ and $9\mu m$ resulting in 28×28 and 32×32 readout images respectively. The qubit atom array is illuminated for a variable readout duration and the scatter photons are collected using EMCCD camera. A total of 14 different readout durations ranging from 15ms to 100ms are used to obtain long-exposure images. Additional path is setup to attenuate the signal by $10\times$ resulting in short-exposure images with effective readout durations ranging from 1.5ms to 10ms.

Training Procedure. Prior to training, all readout images are normalized to ensure consistent scaling, numerical stability, and faster convergence. Each image I_{ij} is zero-centered and normalized according to $I'_{ij} = \frac{I_{ij} - \mu}{I_{\max} - I_{\min}}$, where μ , I_{\max} and I_{\min} are the mean, maximum and minimum pixel intensities in the training subset, respectively. GANDALF uses paired long-exposure and short-exposure images with 65-15-20% as train-validation-test split. The classification models are trained for individual sites in the atom array and uses corresponding site patches of the readout image.

Simulation framework. To evaluate the effect of readout errors on logical error rates of surface codes and BB codes using Stim[12] stabilizer simulator with PyMatching and BP-OSD-CS10 as the respective decoders.

Hardware. We evaluate the inference latency on NVIDIA GeForce RTX 2080 Ti and Intel(R) Xeon(R) Silver 4216 CPU. **Software.** All readout state discriminators are implemented in Python. We use PyTorch framework to build, train, and test all the neural network models in our proposed design.

7 Evaluations

Evaluation metrics. We evaluate GANDALF at three levels: (1) *State Classification*: averaged-site inaccuracy and relative infidelity reduction (η) over the baseline, including post-selection filtering to capture accuracy–latency tradeoffs. (2) *System level*: logical error rate (LER) for surface and bicycle bivariate codes, accounting for idling errors.(3) *QEC cycle latency*: execution-time reduction for QEC codes.

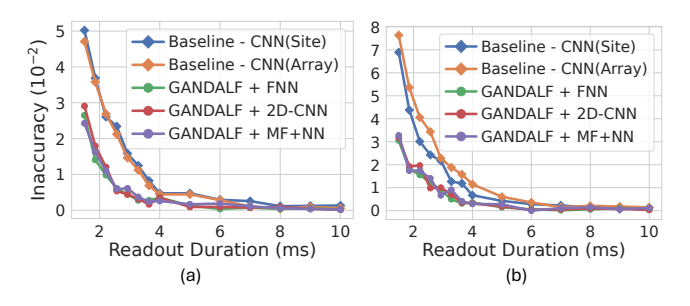


Figure 12. Readout Inaccuracy for (a) $5\mu m$ and (b) $9\mu m$ over all the readout duration ranging from 1.5ms to 10ms.

7.1 Impact on readout accuracy and readout duration

Figure 12 shows the improvement in readout inaccuracy as a function of readout duration for both $5\mu m$ and $9\mu m$ atom spacings. GANDALF delivers substantial gains at short exposure times, where SNR is lowest. Our method achieves $2.8\times$ reduction in readout error compared to the baseline CNN(Site) at 1.5ms. Furthermore, our method sustains below 1% inaccuracy up to 2.9ms for $5\mu m$ and 3.2ms for $9\mu m$, compared to 3.6ms and 4ms for the baseline, respectively. On average, relative infidelity factor, i.e, $\eta = 1 - \delta_{\rm method}/\delta_{\rm CNN(Site)}$, where δ denotes the classification inaccuracy, improves by \sim 64% for atom spacing $5\mu m$ and \sim 53% for $9\mu m$ lattices.

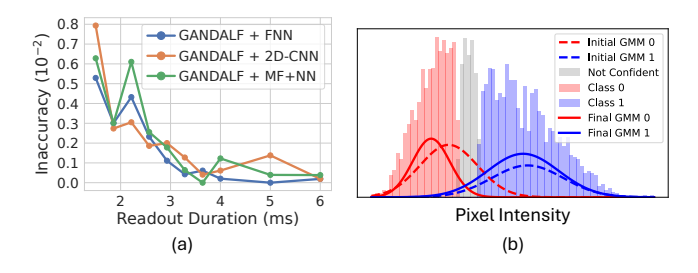


Figure 13. Readout Inaccuracy for post-selected over the shorter readout duration ranging from 1.5*ms* to 6*ms*.

The dataset used in this work is imperfect, but higher-quality data is expected in the near future. To estimate the best-case improvements achievable with denoising, we construct a confidence-filtered dataset using Gaussian Mixture Model (GMM)-based confidence filtering. Instead of relying solely on raw classifier outputs, we fit a two-component GMM to the distribution of decision scores, separating high-confidence bright and dark populations from ambiguous cases as shown in Figure 13(b). By post-selecting only the confident subsets, we maintain sub-1% readout inaccuracy even at the shortest duration of 1.5ms as shown in Figure 13(a). This demonstrates the potential to reduce readout times close to sub-millisecond regime for Cs arrays aiding GANDALF with confidence-aware post-selection.

7.2 Logical error rate

To quantify the end-to-end impact of readout fidelity and latency on fault-tolerant performance, we evaluate logical error rates (LER) using both bivariate bicycle (BB) codes and surface codes (SC). Idling errors during measurement were modeled through the Pauli twirling approximation [32] characterized by T_1 and T_2 times, allowing us to capture the tradeoff between longer readout times with improved accuracy but increased idling error against shorter readout times with reduced idling error but lower accuracy.

Figure 14 indicates an intermediate readout duration of approximately 4ms achieves the best overall LER among the readout durations for 9um, similar trends are observed for 5um. GANDALF-enhanced FNN achieves 5× reduction in

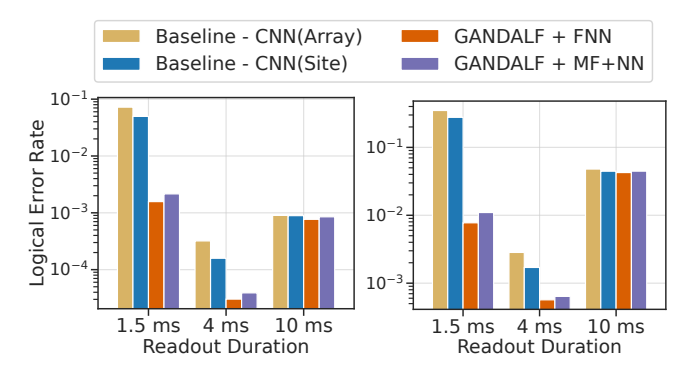


Figure 14. LER for surface d = 11 (left) and BB code d = 12.

LER compared to CNN(Site) baseline at 4ms and upto 35.8× reduction at 1.5ms for BB codes, highlighting the benefits of better readout accuracy at shorter readout duration.

At longer readout times, the gains from higher classification accuracy are outweighed by accumulated idling errors. Conversely, at shorter readout times, insufficient accuracy dominates, leading to higher LER. These results highlight the fundamental tradeoff between readout duration, readout accuracy, and LER, emphasizing the need for optimized readout strategies that balance these competing effects in large-scale neutral atom architectures.

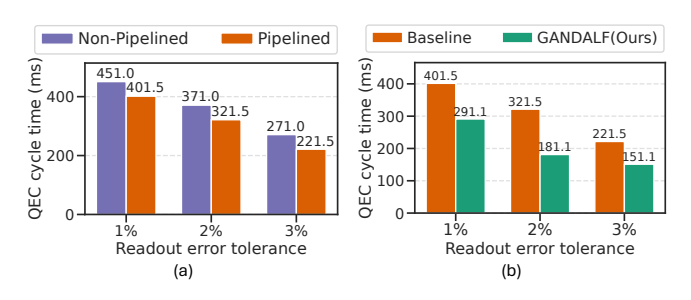


Figure 15. Total QEC Execution time for run for 100 rounds readout error tolerance of 1%, 2% and 3%. (a) Baseline with and without pipelining. (b) Baseline vs GANDALF (ours).

7.3 Reducing QEC cycle latency

Pipelining overlaps denoising and classification with subsequent acquisitions, so their cost is paid only once at the final round. As shown in Fig. 15, this reduces QEC execution time by over 10% (50ms) across 100 rounds, with the largest gains at short readout durations where classification overhead dominates. Incorporating GANDALF further improves performance, achieving up to $1.77\times$ speedup over baseline.

At shortest readout time of 1.5ms, the execution time for 100 rounds decreases from 0.19s with the baseline to 0.152s with GANDALF and pipelining. The advantage grows with number of QEC rounds, as in conventional pipelines, classification adds constant latency with rounds, while the pipelined scheme hids it. As a result, classification never re-emerges

as a bottleneck, when less than readout time, ensuring scalability of real-time QEC to large neutral atom arrays.

8 Conclusions

We present GANDALF, a system architecture that optimizes neutral atom readout by addressing fidelity and latency, the main bottlenecks in scalable quantum error correction. Our framework uses explicit denoising with image translation to reconstruct clear signals from short, low-photon measurements, enabling reliable classification at up to 1.6× shorter readout times. Combined with lightweight classifiers and a pipelined readout design, GANDALF reduces logical error rate by $\sim 35 \times$ for BB code and by $\sim 5 \times$ for Surface code and enables 1.77× lower QEC cycle time compared to state-ofthe-art CNN-based readout for neutral atom arrays. Fully convolutional networks used in our design enable scaling to very large arrays, with batching and parallelism achieving millisecond-level throughput, together establishing a practical path to high-fidelity, low-latency, and scalable readout for large-scale neutral atom processors.

References

[1] Rajeev Acharya, Igor Aleiner, Richard Allen, Trond I. Andersen, Markus Ansmann, Frank Arute, Kunal Arya, Abraham Asfaw, Juan Atalaya, Ryan Babbush, Dave Bacon, Joseph C. Bardin, Joao Basso, Andreas Bengtsson, Sergio Boixo, Gina Bortoli, Alexandre Bourassa, Jenna Bovaird, Leon Brill, Michael Broughton, Bob B. Buckley, David A. Buell, Tim Burger, Brian Burkett, Nicholas Bushnell, Yu Chen, Zijun Chen, Ben Chiaro, Josh Cogan, Roberto Collins, Paul Conner, William Courtney, Alexander L. Crook, Ben Curtin, Dripto M. Debroy, Alexander Del Toro Barba, Sean Demura, Andrew Dunsworth, Daniel Eppens, Catherine Erickson, Lara Faoro, Edward Farhi, Reza Fatemi, Leslie Flores Burgos, Ebrahim Forati, Austin G. Fowler, Brooks Foxen, William Giang, Craig Gidney, Dar Gilboa, Marissa Giustina, Alejandro Grajales Dau, Jonathan A. Gross, Steve Habegger, Michael C. Hamilton, Matthew P. Harrigan, Sean D. Harrington, Oscar Higgott, Jeremy Hilton, Markus Hoffmann, Sabrina Hong, Trent Huang, Ashley Huff, William J. Huggins, Lev B. Ioffe, Sergei V. Isakov, Justin Iveland, Evan Jeffrey, Zhang Jiang, Cody Jones, Pavol Juhas, Dvir Kafri, Kostyantyn Kechedzhi, Julian Kelly, Tanuj Khattar, Mostafa Khezri, Mária Kieferová, Seon Kim, Alexei Kitaev, Paul V. Klimov, Andrey R. Klots, Alexander N. Korotkov, Fedor Kostritsa, John Mark Kreikebaum, David Landhuis, Pavel Laptev, Kim-Ming Lau, Lily Laws, Joonho Lee, Kenny Lee, Brian J. Lester, Alexander Lill, Wayne Liu, Aditya Locharla, Erik Lucero, Fionn D. Malone, Jeffrey Marshall, Orion Martin, Jarrod R. Mc-Clean, Trevor McCourt, Matt McEwen, Anthony Megrant, Bernardo Meurer Costa, Xiao Mi, Kevin C. Miao, Masoud Mohseni, Shirin Montazeri, Alexis Morvan, Emily Mount, Wojciech Mruczkiewicz, Ofer Naaman, Matthew Neeley, Charles Neill, Ani Nersisyan, Hartmut Neven, Michael Newman, Jiun How Ng, Anthony Nguyen, Murray Nguyen, Murphy Yuezhen Niu, Thomas E. O'Brien, Alex Opremcak, John Platt, Andre Petukhov, Rebecca Potter, Leonid P. Pryadko, Chris Quintana, Pedram Roushan, Nicholas C. Rubin, Negar Saei, Daniel Sank, Kannan Sankaragomathi, Kevin J. Satzinger, Henry F. Schurkus, Christopher Schuster, Michael J. Shearn, Aaron Shorter, Vladimir Shvarts, Jindra Skruzny, Vadim Smelyanskiy, W. Clarke Smith, George Sterling, Doug Strain, Marco Szalay, Alfredo Torres, Guifre Vidal, Benjamin Villalonga, Catherine Vollgraff Heidweiller, Theodore White, Cheng Xing, Z. Jamie Yao, Ping Yeh, Juhwan Yoo, Grayson Young, Adam Zalcman, Yaxing Zhang, and Ningfeng Zhu. 2023. Suppressing

- quantum errors by scaling a surface code logical qubit. *Nature* 614, 7949 (Feb. 2023), 676–681. doi:10.1038/s41586-022-05434-1
- [2] Gefen Baranes, Madelyn Cain, J. Pablo Bonilla Ataides, Dolev Bluvstein, Josiah Sinclair, Vladan Vuletic, Hengyun Zhou, and Mikhail D. Lukin. 2025. Leveraging Atom Loss Errors in Fault Tolerant Quantum Algorithms. arXiv:2502.20558 [quant-ph] https://arxiv.org/abs/2502.20558
- [3] Hannes Bernien, Sylvain Schwartz, Alexander Keesling, Harry Levine, Ahmed Omran, Hannes Pichler, Soonwon Choi, Alexander S Zibrov, Manuel Endres, Markus Greiner, et al. 2017. Probing many-body dynamics on a 51-atom quantum simulator. *Nature* 551, 7682 (2017), 579–584
- [4] Dolev Bluvstein, Simon J Evered, Alexandra A Geim, Sophie H Li, Hengyun Zhou, Tom Manovitz, Sepehr Ebadi, Madelyn Cain, Marcin Kalinowski, Dominik Hangleiter, et al. 2024. Logical quantum processor based on reconfigurable atom arrays. *Nature* 626, 7997 (2024), 58–65.
- [5] Neng-Chun Chiu, Elias C Trapp, Jinen Guo, Mohamed H Abobeih, Luke M Stewart, Simon Hollerith, Pavel Stroganov, Marcin Kalinowski, Alexandra A Geim, Simon J Evered, et al. 2025. Continuous operation of a coherent 3,000-qubit system. arXiv preprint arXiv:2506.20660 (2025).
- [6] M. N. H. Chow, B. J. Little, and Y.-Y. Jau. 2023. High-fidelity low-loss state detection of alkali-metal atoms in optical tweezer traps. *Phys. Rev.* A 108 (Sep 2023), 032407. Issue 3. doi:10.1103/PhysRevA.108.032407
- [7] J. P. Covey, I. S. Madjarov, A. Cooper, and M. Endres. 2019. 2000-times repeated imaging of Strontium atoms in clock-magic tweezer arrays. *Phys. Rev. Lett.* 122 (2019), 173201.
- [8] M. Endres, M. Cheneau, T. Fukuhara, C. Weitenberg, P. Schauß, C. Gross, L. Mazza, M. C. Bañuls, L. Pollet, I. Bloch, and S. Kuhr. 2013. Single-site- and single-atom-resolved measurement of correlation functions. *Applied Physics B* 113, 1 (Aug. 2013), 27–39. doi:10.1007/s00340-013-5552-9
- [9] A. Fuhrmanek, R. Bourgain, Y. R. P. Sortais, and A. Browaeys. 2011. Free-space lossless state detection of a single trapped atom. *Phys. Rev. Lett.* 106 (2011), 133003.
- [10] György P. Gehér, Marcin Jastrzebski, Earl T. Campbell, and Ophelia Crawford. 2025. To reset, or not to reset—that is the question. npj Quantum Information 11, 1 (07 Mar 2025), 39. doi:10.1038/s41534-025-00998-v
- [11] M. J. Gibbons, C. D. Hamley, C.-Y. Shih, and M. S. Chapman. 2011. Non-destructive fluorescent state detection of single neutral atom qubits. *Phys. Rev. Lett.* 106 (2011), 133002.
- [12] Craig Gidney. 2021. Stim: a fast stabilizer circuit simulator. Quantum 5 (July 2021), 497. doi:10.22331/q-2021-07-06-497
- [13] Craig Gidney. 2025. How to factor 2048 bit RSA integers with less than a million noisy qubits. arXiv preprint arXiv:2505.15917 (2025).
- [14] TM Graham, Y Song, J Scott, C Poole, L Phuttitarn, K Jooya, P Eichler, X Jiang, A Marra, B Grinkemeyer, et al. 2022. Multi-qubit entanglement and algorithms on a neutral-atom quantum computer. *Nature* 604, 7906 (2022), 457–462.
- [15] W. Huie, L. Li, N. Chen, X. Hu, Z. Jia, W. K. C. Sun, and J. P. Covey. 2023. Repetitive readout and real-time control of nuclear spin qubits in ¹⁷¹Yb atoms. *PRX Quantum* 4 (Sep 2023), 030337. Issue 3. doi:10. 1103/PRXQuantum.4.030337
- [16] L Isenhower, E Urban, XL Zhang, AT Gill, T Henage, TG Walker, and M Saffman. 2010. Demonstration of a neutral atom controlled-NOT quantum gate. *Physical review letters* 104, 1 (2010), 010503.
- [17] Phillip Isola, Jun-Yan Zhu, Tinghui Zhou, and Alexei A Efros. 2017. Image-to-Image Translation with Conditional Adversarial Networks. CVPR (2017).
- [18] M. Kwon, M. F. Ebert, T. G. Walker, and M. Saffman. 2017. Parallel low-loss measurement of multiple atomic qubits. *Phys. Rev. Lett.* 119 (2017), 180504.

- [19] Harry Levine, Alexander Keesling, Giulia Semeghini, Ahmed Omran, Tout T Wang, Sepehr Ebadi, Hannes Bernien, Markus Greiner, Vladan Vuletić, Hannes Pichler, et al. 2019. Parallel implementation of highfidelity multiqubit gates with neutral atoms. *Physical review letters* 123, 17 (2019), 170503.
- [20] J. W. Lis, A. Senoo, W. F. McGrew, F. Rönchen, A. Jenkins, and A. M. Kaufman. 2023. Mid-circuit operations using the omg-architecture in neutral atom arrays. *Phys. Rev. X* 13 (Dec 2023), 041035. Issue 4. doi:10.1103/PhysRevX.13.041035
- [21] S. Ma, G. Liu, P. Peng, B. Zhang, S. Jandura, J. Claes, A. P. Burgers, G. Pupillo, S. Puri, and J. D. Thompson. 2023. High-fidelity gates and mid-circuit erasure conversion in an atomic qubit. *Nature* 622 (Oct 2023), 279–284. Issue 7982. doi:10.1038/s41586-023-06585-6
- [22] Ivaylo S. Madjarov, Jacob P. Covey, Adam L. Shaw, Joonhee Choi, Anant Kale, Alexandre Cooper, Hannes Pichler, Vladimir Schkolnik, Jason R. Williams, and Manuel Endres. 2020. High-fidelity entanglement and detection of alkaline-earth Rydberg atoms. *Nature Physics* 16, 8 (May 2020), 857–861. doi:10.1038/s41567-020-0903-z
- [23] M. Martinez-Dorantes, W. Alt, J. Gallego, S. Ghosh, L. Ratschbacher, Y. Völzke, and D. Meschede. 2017. Fast nondestructive parallel readout of neutral atom registers in optical potentials. *Phys. Rev. Lett.* 119 (2017), 180503.
- [24] Matthew A. Norcia, Hyemin Kim, William B. Cairncross, Simon de Léséleuc, Daniel Henneke, Harry Levine, , Marric Stephens, , Mark Saffman, , and Alexandre Doret. 2024. Iterative Assembly of ¹⁷¹Yb Atom Arrays with Cavity-Enhanced Optical Lattices. *PRX Quantum* 5, 3 (2024), 030316. doi:10.1103/PRXQuantum.5.030316
- [25] L. Phuttitarn, B. M. Becker, R. Chinnarasu, T. M. Graham, and M. Saffman. 2024. Enhanced measurement of neutral-atom qubits with machine learning. *Physical Review Applied* 22, 2 (Aug. 2024). doi:10. 1103/physrevapplied.22.024011
- [26] Mark Saffman. 2019. Quantum computing with neutral atoms. National Science Review 6, 1 (2019), 24–25.
- [27] M Saffman. 2025. Quantum computing with atomic qubit arrays: confronting the cost of connectivity. arXiv preprint arXiv:2505.11218 (2025).
- [28] Pedro Sales Rodriguez, John M Robinson, Paul Niklas Jepsen, Zhiyang He, Casey Duckering, Chen Zhao, Kai-Hsin Wu, Joseph Campo, Kevin Bagnall, Minho Kwon, et al. 2025. Experimental demonstration of logical magic state distillation. *Nature* (2025), 1–3.
- [29] S. Saskin, J. T. Wilson, B. Grinkemeyer, and J. D. Thompson. 2019. Narrow-Line Cooling and Imaging of Ytterbium Atoms in an Optical Tweezer Array. *Phys. Rev. Lett.* 122 (Apr 2019), 143002. Issue 14. doi:10.1103/PhysRevLett.122.143002
- [30] M. E. Shea, P. M. Baker, J. A. Joseph, J. Kim, and D. J. Gauthier. 2020. Submillisecond, nondestructive, time-resolved quantum-state readout of a single, trapped neutral atom. *Phys. Rev. A* 102 (2020), 053101.
- [31] R. Tao, M. Ammenwerth, F. Gyger, I. Bloch, and J. Zeiher. 2024. High-fidelity detection of large-scale atom arrays in an optical lattice. *Phys. Rev. Lett.* 133 (Jul 2024), 013401. Issue 1. doi:10.1103/PhysRevLett.133. 013401
- [32] Yu Tomita and Krysta M. Svore. 2014. Low-distance surface codes under realistic quantum noise. *Physical Review A* 90, 6 (Dec. 2014). doi:10.1103/physreva.90.062320
- [33] Karen Wintersperger, Florian Dommert, Thomas Ehmer, Andrey Hoursanov, Johannes Klepsch, Wolfgang Mauerer, Georg Reuber, Thomas Strohm, Ming Yin, and Sebastian Luber. 2023. Neutral atom quantum computing hardware: performance and end-user perspective. EPJ Quantum Technology 10, 1 (Aug. 2023). doi:10.1140/epjqt/s40507-023-00190-1
- [34] Karen Wintersperger, Florian Dommert, Thomas Ehmer, Andrey Hoursanov, Johannes Klepsch, Wolfgang Mauerer, Georg Reuber, Thomas Strohm, Ming Yin, and Sebastian Luber. 2023. Neutral atom quantum computing hardware: performance and end-user perspective. EPJ

- Quantum Technology 10, 1 (2023), 32.
- [35] T.-Y. Wu, A. Kumar, F. Giraldo, and D. S. Weiss. 2019. Stern-Gerlach detection of neutral-atom qubits in a state-dependent optical lattice. *Nat. Phys.* 15 (2019), 538.